

A numerical evaluation of flows through an SMX-Plus mixer

Fouad Azizi, Walid Abou-Hweij, Noureddine Lebaz, Nida Sheibat-Othman

▶ **To cite this version:**

Fouad Azizi, Walid Abou-Hweij, Noureddine Lebaz, Nida Sheibat-Othman. A numerical evaluation of flows through an SMX-Plus mixer. Chemical Engineering Research and Design, 2022, 178, pp.382-394. 10.1016/j.cherd.2021.12.030 . hal-03518109

HAL Id: hal-03518109
https://hal.science/hal-03518109

Submitted on 14 Oct 2022

HAL is a multi-disciplinary open access archive for the deposit and dissemination of scientific research documents, whether they are published or not. The documents may come from teaching and research institutions in France or abroad, or from public or private research centers.

L'archive ouverte pluridisciplinaire **HAL**, est destinée au dépôt et à la diffusion de documents scientifiques de niveau recherche, publiés ou non, émanant des établissements d'enseignement et de recherche français ou étrangers, des laboratoires publics ou privés.

A numerical evaluation of flows through an SMX-Plus mixer

Fouad Azizi[1*]; Walid Abou-Hweij[1]; Noureddine Lebaz[2]; Nida Sheibat-Othman[2]

[1] *B.&W. Bassatne Department of Chemical Engineering and Advanced Energy, American University of Beirut, PO Box 11-0236, Riyad El-Solh, Beirut, Lebanon*

[2] *University of Lyon, Université Claude Bernard Lyon 1, CNRS, LAGEPP UMR 5007, F-69100, Villeurbanne, France*

Abstract

A numerical investigation of the flow through an SMX+ mixer was undertaken in this study. Three mixer elements were placed in series and various hydrodynamic parameters were assessed. The study considered a single-phase flow of different viscosity flowing at a hydraulic Reynolds number between 220 and 660 which ensured turbulent conditions within the mixer. The data was subjected to a grid-independence study and validated against pressure drop measurements collected under a wide range of hydrodynamic conditions.

The results show that a three-dimensional velocity field dominates the flow within the mixer where the distribution of the strain rate and vorticity magnitudes undergo large fluctuations. The extensional efficiency was found to increase substantially in the first part of the mixer which indicates good dispersive behavior, however, this value decreases continuously as the flow exits the mixer and reaches values below 0.5 downstream of the last element. This was due to the presence of a significant rotational core as the fluid flows farther away of the last mixer. This also explained the persistence of a flatter velocity profile downstream of the mixing section. Finally, the energy dissipation rate and kinetic energy were also studied and the contribution of the mean flow was found to be significantly larger than the turbulence contribution under the investigated conditions.

Keywords: SMX+, static mixer, extensional efficiency, helicity, turbulence, pressure drop.

[*] *Corresponding author*: *Telephone: +961-1-374374, ext: 3439; email: fouad.azizi@aub.edu.lb*

1 Introduction

The use of static mixers in the chemical industry has become common practice as they allow transforming pipelines into mixing vessels (Kresta et al., 2016) thereby reducing the need for large reactor/contactor volumes. A plethora of commercial designs is available on the market and there is a growing number of investigations in the open literature that proposes new designs (Vikhansky, 2020) (or modifications to existing ones). The latter phenomenon goes in parallel with the advances in computational fluid dynamics (CFD) as it allows easier testing and characterization of these new geometries. For a comprehensive review of static mixers and their applications, the reader is referred to the reviews of Thakur et al. (Thakur et al., 2003), and Ghanem et al. (Ghanem et al., 2014).

One variant of these static mixers is the SMX family of mixers (SMX^{TM} or SMX+^{TM}) developed by Sulzer (Hirschberg et al., 2009). These mixers have been used to promote multiphase flow dispersions either in laminar or turbulent regimes (Hirschberg et al., 2009; Leclaire et al., 2020; Theron et al., 2010). These mixers are characterized by having various bars placed in a X-shaped geometry with the SMX+ mixer having a lesser number and a reduced pressure drop because of its thinner lamella (Chabanon et al., 2017; Hirschberg et al., 2009).

To characterize the hydrodynamics of flows through such geometries (or other static mixers), experimental techniques are not always capable of rendering local flow information with a good accuracy (Leclaire et al., 2020). This is due to the complex three-dimensional structures and chaotic flow patterns. For this, CFD offers an advantage whereby local information can be obtained regardless of the complexity of the flow which allows a more detailed analysis of the processes (Haddadi et al., 2020; Leclaire et al., 2020).

A search of the open literature renders various numerical studies that characterized the single- and two-phase flows in SMX mixers (Haddadi et al., 2020; Jegatheeswaran et al., 2018; Leclaire et al., 2020; Liu et al., 2006; Pianko-Oprych and Jaworski, 2010; Rauline et al., 2000, 1998). To the authors best knowledge, CFD studies for the SMX+ geometry are almost inexistent, with the study of Hirschberg et al. (Hirschberg et al., 2009) and Meijer et al. (Meijer et al., 2012) being the only available ones. Hirschberg et al. (Hirschberg et al., 2009) conducted laser-induced fluorescence (LIF) experiments, decolorization tests, and CFD simulations to characterize the pressure drop and mixing quality in the mixer. However, Meijer et al. (Meijer et al., 2012) performed 3D CFD simulations to characterize mixing by means of the flux-weighted area-averaged intensity of segregation and concluded that unlike the findings of

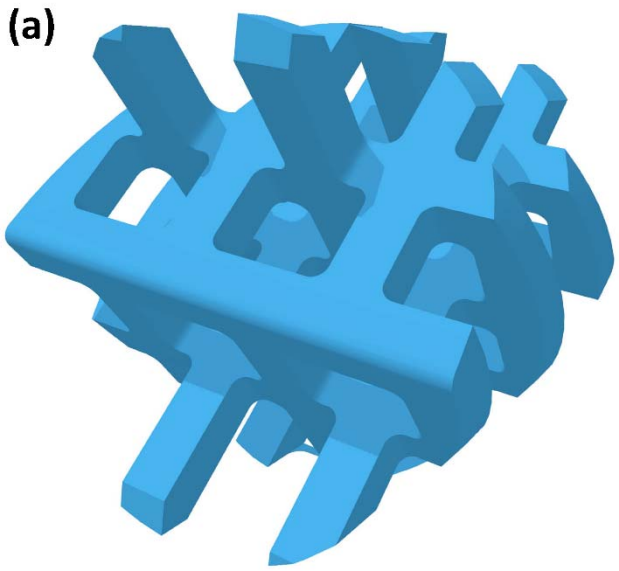
Hirschberg et al. (Hirschberg et al., 2009), the SMX+ enhances the mixing when compared to the standard SMX mixer.

Accordingly, the aim of this work is to conduct a numerical study to characterize the single-phase flow hydrodynamics through SMX+ mixers. It will be the first study that details the velocity field in these geometries as well as the various turbulence characteristics.

2 Methodology

2.1 Computational domain

The computational domain consists of a circular pipe of internal diameter, D = 4.8 mm and length, $L_p = 15D$. Three mixer elements were inserted in one row inside this pipe with the first element being at a distance of $3D$ from the inlet. These elements have a diameter equal to that of the circular pipe and an aspect ratio (L_m/D) equals to 1, with L_m being the mixer length. The mixer elements were rotated counter-clockwise at 45° with respect to each other.



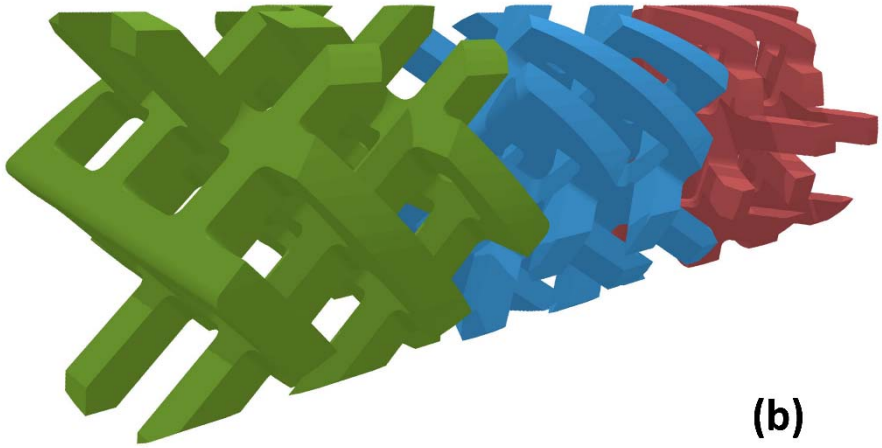


Figure 1: Geometry of the SMX+ mixer: (a) one mixer element, (b) 3 elements in a row.

The SMX+ geometry that was provided by Sulzer is shown in Figure 1a. Figure 1b presents the 3 elements in a row. It should be noted that simulations with 5 consecutive elements were also conducted but the flow field was found to be repetitive after the second element. For this reason, the current simulations were conducted with only 3 mixer elements.

Experimental data for validation of the pressure drop (Δp) is available for water-glycerol mixtures of varying densities and viscosities. For this reason, the simulations were set up using a single-phase fluid having a density and viscosity similar to the mixture properties. The conditions investigated here replicate the flows utilized in the studies of Lebaz and Sheibat-Othman (Lebaz and Sheibat-Othman, 2019a, 2019b). In these investigations, Lebaz and Sheibat-Othman (Lebaz and Sheibat-Othman, 2019b, 2019a) studied the effect of changing the continuous phase viscosity and velocity on the breakage of dilute (i.e., 1 wt%) liquid-liquid dispersions in SMX+ static mixers. A large database of experimental measurements of Δp as a function of viscosity and velocity is therefore available.

For the current study, the effect of changing the flow velocity at constant fluid properties or changing the fluid properties and velocity while maintaining the same Reynolds number, were considered. The conditions that will be investigated here to study the flow field are shown in Table 1. These conditions were selected as representative of various water-glycerol mixtures (more on this in the model validation section). This table shows in addition to the viscosity (μ), density (ρ), and average velocity (U_{avg}), both the pipe and hydraulic Reynolds numbers, Re_{pipe} and Re_h, respectively. The latter parameter is defined according to Equation (1),

$$\mathrm{Re_h} = \frac{\rho \cdot U_{\mathrm{avg}} \cdot D_{\mathrm{h}}}{\mu \cdot \varphi} \quad (1)$$

where D_{h} is the hydraulic diameter inside the static mixer and φ is the porosity of the mixer. For the mixer used in the current study, $D_{\mathrm{h}} = 1.96\times10^{-3}$ m and $\varphi = 0.75$.

Table 1: Operating conditions investigated in the current study.

Case Nb.	μ **(mPa·s)**	ρ **(kg/m^3)**	U_{avg} **(m/s)**	$\mathbf{Re}_{pipe}$	$\mathbf{Re}_{h}$
1	2.5	1076	0.194	400	220
2	2.5	1076	0.356	735	400
3	2.5	1076	0.586	1190	660
4	7.5	1136	1.011	735	400
5	11.56	1155	1.532	735	400

The computational domain was discretized using an unstructured tetrahedral grid scheme using the automatic meshing tool available in the commercial software ANSYS®. In order to provide proper geometric discretization for the flow domain while capturing both its small and large geometric features, the domain was divided into three main regions, namely, the open-pipe, near-mixer, and mixer regions. The latter volume was the most refined region followed by the near-mixer region while the coarsest mesh was employed in the open-pipe region. Figure 2a illustrates the various grid levels allocated for the different regions of the computational domain through the central XY-plane. The near mixer region was used to capture the expected fluctuation and flow circulations upstream and downstream of the mixers zone. The upstream (near-mixer) region was fixed at 0.5*D* in length, while the downstream region extended to 1.5*D*. Figure 2b presents the surface grid discretization of the SMX+ mixer.

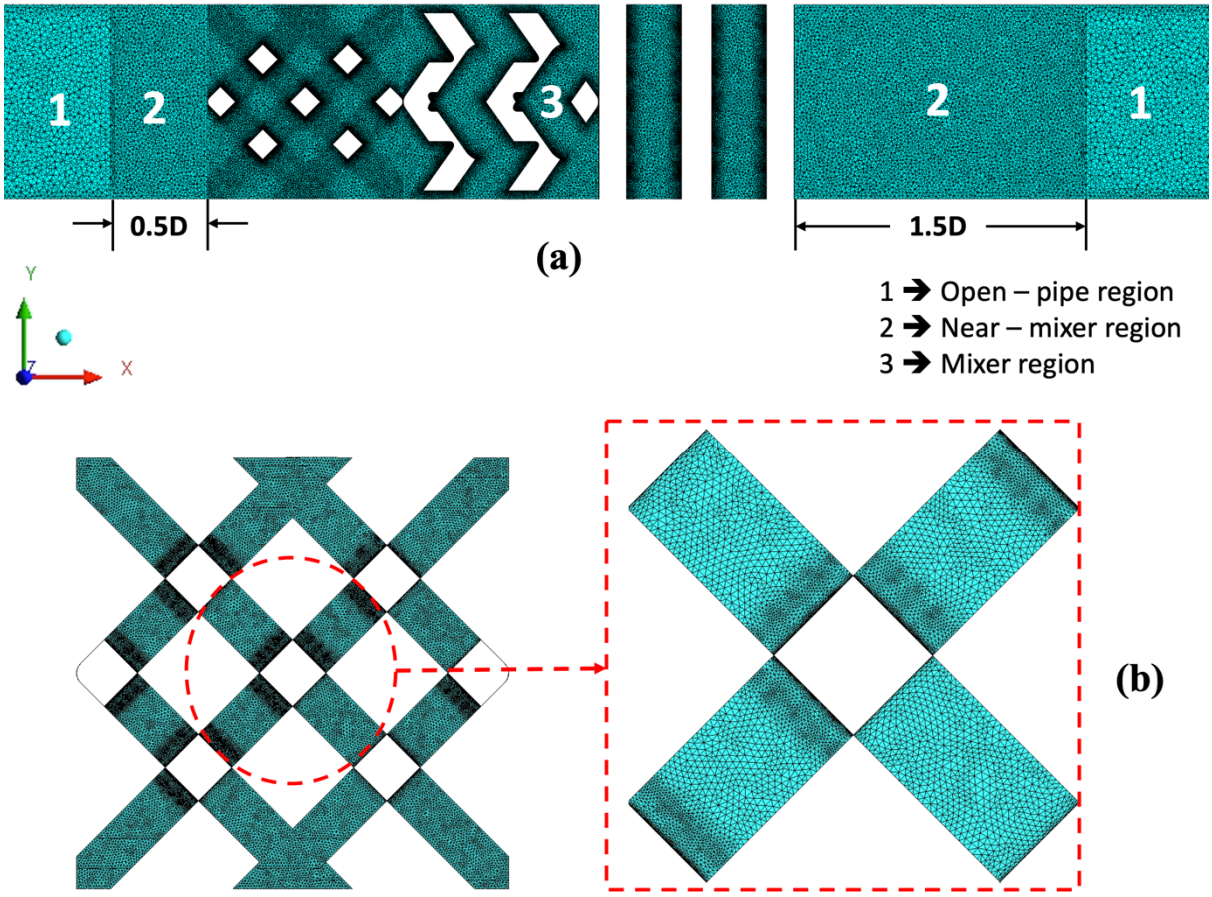


Figure 2: Meshing configuration (a) along the central *xy*-plane and (b) surface grid generation for SMX+ mixer.

2.2 Boundary conditions and solution method

The current investigated conditions fall under a purely laminar flow in the empty pipe region, however, the flow in the interstitial space between the mixer blades is expected to be turbulent. Theron and Le Sauze (Theron and Sauze, 2011) reported that turbulent flow in the SMX+ mixer appears at around Re_h = 260. While the SMX+ static mixer was subject to laminar flow conditions $Re_{pipe} \leq 2300$ (c.f. Table 1), turbulent field involving circulations and vortices could be generated within the flow. To be able to predict turbulence with low computational cost, the Reynolds-Averaged Navier-Stokes (RANS) equation was used. Thus, for a steady incompressible and Newtonian fluid in the absence of any external body forces, the mean mass and momentum conservation equations reduced to Equations (2) and (3), respectively.

$$\frac{\partial \langle U_i \rangle}{\partial x_i} = 0 \tag{2}$$

$$\langle U_j \rangle \frac{\partial \langle U_i \rangle}{\partial x_j} = -\frac{1}{\rho}\frac{\partial p}{\partial x_i} + \nu \frac{\partial^2 \langle U_i \rangle}{\partial x_j \partial x_j} - \frac{\partial \langle u_i' u_j' \rangle}{\partial x_j} \tag{3}$$

$$U_i = \langle U_i \rangle + u_i' \tag{4}$$

where $\langle U_i \rangle$ and u_i' are the mean and fluctuating velocity components of the instantaneous velocity U_i $(i = x, y, z)$, p is the static pressure, ν is the kinematic viscosity $(\nu = \mu/\rho)$, and $-\langle u_i' u_j' \rangle$ is the Reynolds stress tensor.

The Reynolds stress tensor was solved using the Boussinesq eddy-viscosity hypothesis (Hinze, 1959). This tensor was set proportional to the mean velocity gradient with the constant of proportionality being the turbulent viscosity, μ_t. For an incompressible fluid, the Reynolds stress term is given by Equation (5).

$$-\langle u_i' u_j' \rangle = \nu_t \left(\frac{\partial \langle U_i \rangle}{\partial x_j} + \frac{\partial \langle U_j \rangle}{\partial x_i} \right) - \frac{2}{3} k_t \delta_{ij} \tag{5}$$

$$k_t = \frac{1}{2} \langle u_i' u_i' \rangle \tag{6}$$

where k_t is the turbulent kinetic energy given by Equation (6) and ν_t is the turbulent kinematic viscosity $(\nu_t = \mu_t/\rho)$.

Different eddy-viscosity models are available in the literature. In this study, the "realizable" *k-ε* turbulence model was used because of its suitability to complex shear flows involving rapid strain and vortices and strong streamline curvature conditions, that are present in the current mixer. It should be noted that validation of the turbulence model is outside the scope of the current work. However, literature information recommend the use of the *k-ε* family of models (standard or realizable) as they render similar results (Coroneo et al., 2012).

Ansys Fluent® which is a finite-volume solver was used in the current study. A fully developed laminar velocity profile was imposed at the inlet using a user-defined function (UDF), while the outlet was set to the outflow boundary condition. In addition, the no-slip boundary condition was used for the solid walls of both the pipe and the mixer elements. The solution methods used in the current study are listed in Table 2.

Table 2: Solution methods used in the current study.

Solver	Pressure based
Pressure-velocity coupling	SIMPLE algorithm
Gradient terms	Least-square cell based

Convection terms	QUICK
Pressure interpolation	2nd order
Residuals	$< 10^{-6}$

2.3 Grid independence

The grid convergence index method (GCI) proposed by Celik et al. (Celik et al., 2008) was used to study the grid independence of the solution. Three different grid levels were tested and different flow parameters including the pressure drop, local and volume average turbulence quantities (i.e., k and ε) were selected for predicting grid independency. Table 3 presents the total number of grid cells, N_e, for the various grid levels as well as their corresponding GCI values. Hence, the fine grid of approximately 22.3 million cells was selected. It should be noted that the number of grid cells represents the total number within the whole computational domain. For this fine grid, each mixer element was divided into about 6 million grid cells. The numerical simulations were then performed on a high-performance computing (HPC) cluster using four parallel nodes each of 16 processors and 64 GB RAM of Intel® Xeon® Processor E5-2665 @ 2.4 GHz.

Table 3: Grid independence test for the studied static mixer

Refinement Level	Number of grid cells, N_e	GCI %
Fine	22,333,325	1.39
Medium	8,468,669	3.78
Coarse	3,613,183	-

3 Results

The outcome of the simulations will be presented in this section. The model validation will be first presented then followed by a discussion about the velocity and turbulence fields inside the mixers.

3.1 Pressure Drop – Model validation

To validate the current approach, the numerical results were compared against pressure drop data taken from the work of Lebaz and Sheibat-Othman (Lebaz and Sheibat-Othman, 2019b, 2019a). In their attempt to study liquid-liquid emulsification in SMX+ mixers, Lebaz and Sheibat-Othman (Lebaz and Sheibat-Othman, 2019b, 2019a) conducted experiments using 10

SMX+ elements at very low dispersed phase volume fractions while varying the continuous phase viscosity by adding glycerol to water.

The current simulations were therefore conducted using a single fluid, the properties of which are set as equivalent to the apparent viscosity and density of the mixtures. As such, 9 pressure drop measurements representing a wide array of fluid viscosities (ranging between 1 and 21.77 mPa·s), densities (998.2 – 1181.4 kg/m^3), and Re_h (87 – 1,510) were used to test the validity of the current approach. For these conditions, the empty pipe Reynolds number, Re_{pipe} ranged between 160 and 2,770.

The data was compared based on the pressure drop across one single mixer element. The predicted pressure drop across one element, Δp_e, is compared to the experimentally measured values in Figure 3. From these figures it can be observed that the CFD predictions matched well the experimental data points. Figure 3a shows the variation of the pressure drop across one element with the fluid viscosity while Figure 3b is a parity plot that highlights the spread of the predictions. The mean relative error between the experimental and predicted values was found to be 13.8% while the maximum and minimum deviations were recorded at 32% and 4.2% respectively. Figure 3b clearly shows that most of the data points fell within ± 20% of the measured values which is a good measure of the validity of the current approach.

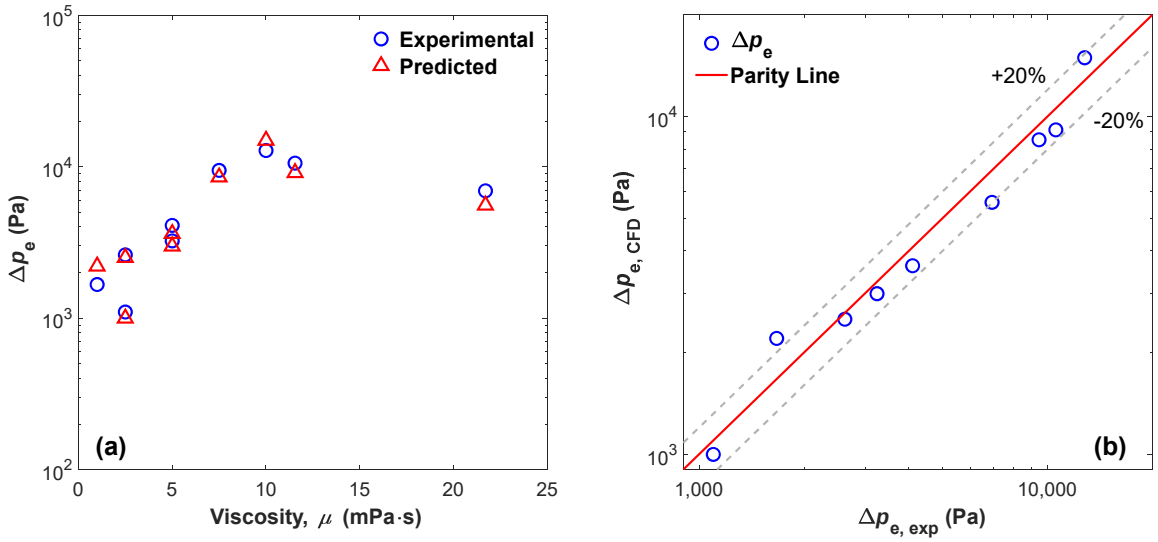


Figure 3: Validation of numerical simulations. (a) pressure drop across one element vs. viscosity; (b) parity plot of Δp_e for predictions vs experimental measurements.

3.2 Hydrodynamic characterization

To better characterize the hydrodynamics of the flow through SMX+ mixers, knowledge of the velocity field is important as it helps identify regions of interest, such as recirculation zones and flow irregularities. In the current work, the effect of changing the flow velocity and fluid viscosity were investigated, and the results will be presented in terms of the velocity components, strain rate, vorticity, and extensional efficiency. In addition, the helicity as well as the turbulence field characteristics, namely, kinetic energy and energy dissipation rates, will be presented.

3.2.1 Velocity Field

The solution of the equations of motion in the current computational domain provides the velocity field for the flowing fluid. Figure 4 shows the streamlines of the flow as it passes through the series of SMX+ mixers for Case # 2. It shows the streamlines with and without the presence of the mixer bars for better visualization of the flow inside the volume of the elements. It can be clearly discerned that the flow is rotated inside the mixer and goes through regions of high velocity and others of low velocity as it travels around the bars of the mixer.

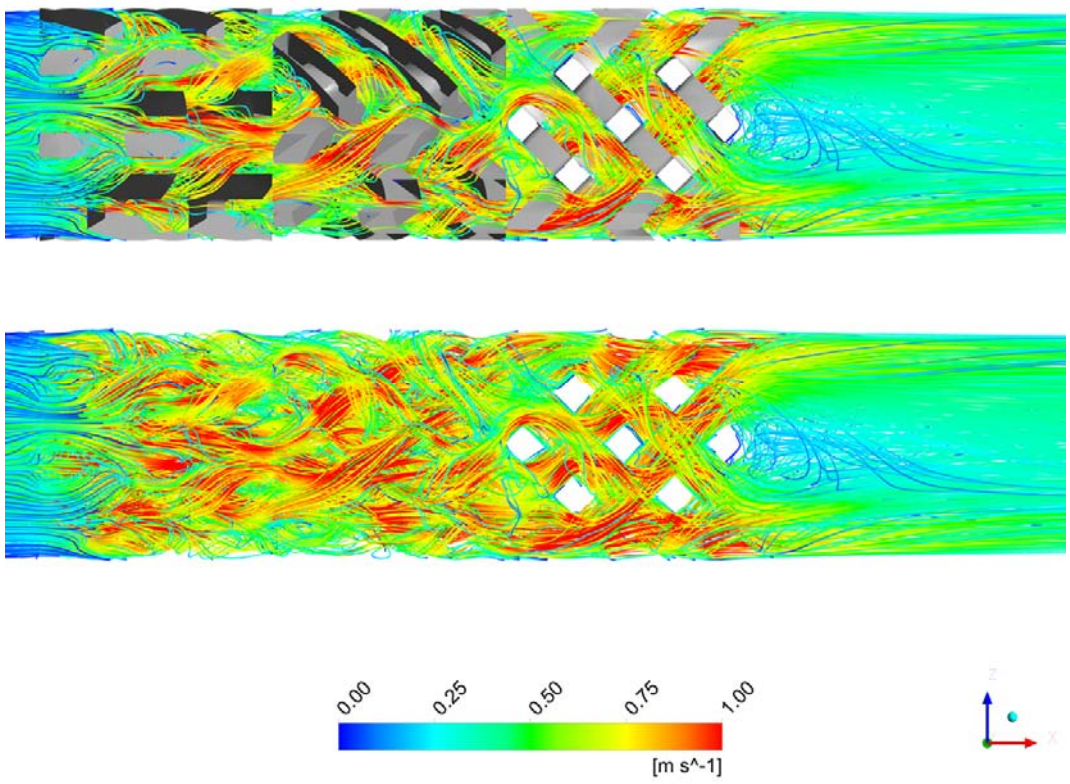


Figure 4: Streamlines of the flow velocity through the SMX+ mixer for Case # 2 (U_{avg} = 0.356 m/s, μ = 2.5 mPa·s, Re_h = 400). Picture showing the streamlines with and without the mixer bars.

Figure 5 is a composite figure that shows the contour plots for different variables as the flow is passing through the second SMX+ element in the series. The data is extracted for Case # 4 (i.e., U_{avg} = 1.011 m/s, Re_h = 400). These plots are shown at different dimensionless lengths, L^*. This length has been non-dimensionalized between 0 and 1, whereby a value of L^* = 0 indicates the inlet to the 2nd mixer, while L^* = 1 corresponds to the outlet of the 2nd mixing element.

The first column of Figure 5 shows the contour plots of the axial velocity component, $\langle U_x \rangle$ with the radial and tangential components (i.e, $\langle U_y \rangle$ and $\langle U_z \rangle$) overlaid as vectors. The size of these vectors is proportional to their magnitude. From these contours, it can be clearly observed that the flow accelerates substantially as it passes through the mixer with the radial and tangential components being significant inside of it, which indicates rigorous mixing of the fluid elements. This effect is further confirmed when considering the second column of Figure 5. In it, the surface streamlines are colored by the magnitude of the axial vorticity, $\langle \omega_x \rangle$. In these plots, and for a better visualization, the positive values of the axial vorticity that indicate counter-clockwise swirl rotation were colored in red, while the negative values that represent a clockwise swirl rotation were colored in blue. These plots reveal that both positive and negative vorticity is produced in the mixer. The flow enters the mixer with two pairs of vortices in the clockwise direction that quickly subside and form two main counter-clockwise vortices inside the mixer. The flow exits the mixing element by re-forming the two pairs of clockwise vortices. Such changes in the direction of the swirl and the complexity of the secondary flow are an indication of good radial mixing within the SMX+.

The third and fourth columns of Figure 5 show the contour plots of the magnitude of mean rate of strain tensor, $|\bar{S}_{ij}|$, and the magnitude of the mean vorticity tensor, $|\bar{\Omega}_{ij}|$, respectively. These parameters are computed following equations (7) to (10), where $\bar{S}_{ij}$ is the mean rate of strain tensor and $\bar{\Omega}_{ij}$ is the mean vorticity tensor. It can be clearly observed that the strain rate distribution is non-uniform within the mixer volume, although it is highest on the solid walls of either the pipe or the mixer crossbars.

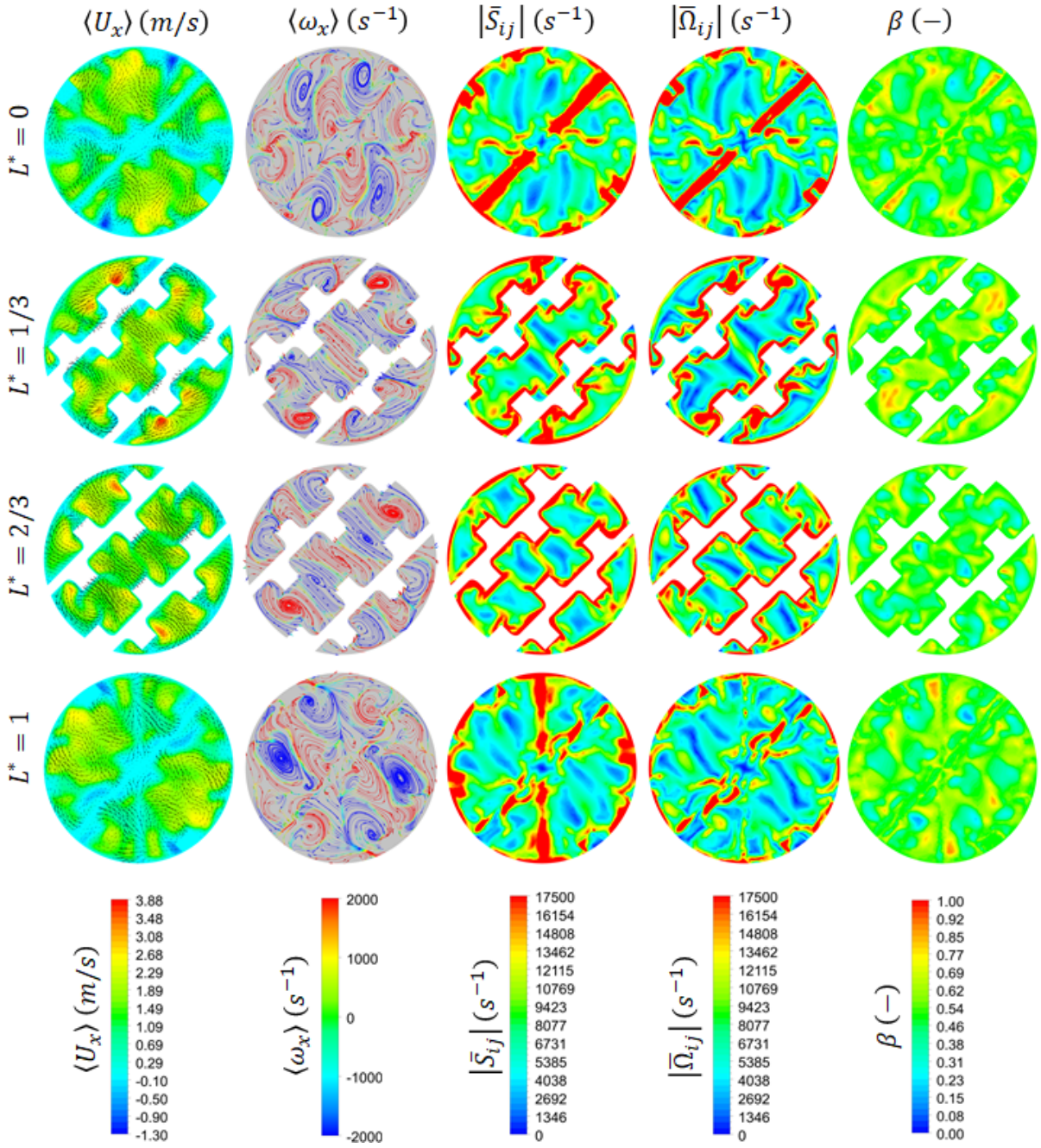


Figure 5: Contour plots for various parameters of the flow field within the 2nd mixer element for Case # 4. Columns left to right: velocity field, surface streamlines colored by the axial vorticity $\langle \omega_x \rangle$, magnitude of the mean rate of strain tensor $|\bar{S}_{ij}|$, magnitude of the mean vorticity tensor $|\bar{\Omega}_{ij}|$, and extensional efficiency β.

This is expected as the maximum velocity gradients exist in these regions. However, one cannot but notice the existence of regions of very low levels of strain rates inside the mixer which is an indication of poor mixing in these regions. This observation is in line with the observations of Liu et al. (Liu et al., 2006) who reported a similar behavior for the SMX mixers.

$$\bar{S}_{ij} = \frac{1}{2}\left(\frac{\partial\langle U_i\rangle}{\partial x_j} + \frac{\partial\langle U_j\rangle}{\partial x_i}\right) \tag{7}$$

$$\bar{\Omega}_{ij} = \frac{1}{2}\left(\frac{\partial\langle U_i\rangle}{\partial x_j} - \frac{\partial\langle U_j\rangle}{\partial x_i}\right) \tag{8}$$

$$\left|\bar{S}_{ij}\right| = \sqrt{2\bar{S}_{ij}\bar{S}_{ij}} \tag{9}$$

$$\left|\bar{\Omega}_{ij}\right| = \sqrt{2\bar{\Omega}_{ij}\bar{\Omega}_{ij}} \tag{10}$$

The contours of the magnitude of the vorticity tensor also show the regions of maximal and minimal vorticity in these mixers. The highest values of $\left|\bar{\Omega}_{ij}\right|$ correspond to regions of high vorticity irrespective of whether the vorticity is positive or negative. Hence, the regions of very low magnitude are those where the axial vorticity is negligible (cf. interface between clockwise and counter-clockwise swirls in the second column of Figure 5). One should keep in mind that the magnitude of the vorticity tensor cannot be employed to identify vortex cores in a shear flow (Jeong and Hussain, 1995).

3.2.2 Extensional efficiency

The fifth column of Figure 5 shows the contour plots of the extensional efficiency, β, as the flow passes through the mixer. Introduced by Manas-Zloczower (Manas-Zloczower, 1994) to assess the dispersive mixing efficiency, this parameter quantifies the relative importance of extensional over rotational effects of the flow (de la Villéon et al., 1998). The extensional efficiency, β, can be computed following Equation (11), where a value of $\beta = 1$ indicates pure elongation, $\beta = 0$ represents pure rotation, and $\beta = 0.5$ indicates simple shear flow.

$$\beta = \frac{\left|\bar{S}_{ij}\right|}{\left|\bar{S}_{ij}\right| + \left|\bar{\Omega}_{ij}\right|} \tag{11}$$

From the contour plots it can be discerned that the "entrance" region in the mixer is characterized by large values of β which can be attributed to the fact that the fluid elements have to be stretched and elongated to pass through the interstitial openings of the SMX+. The effect of this elongation and stretching reduces once the flow is inside the mixer volume where it reverts to a simple shear flow.

This behavior is further highlighted in Figure 6 which presents the variation of the extensional efficiency along the computational domain. The abscissa (x-axis) represents the physical

distance from the inlet, while the ordinate (y-axis) is the average extensional efficiency at a cross-sectional plane located at the given distance. The mixing elements are overlaid on these figures to show the physical location of the mixers with respect to the data. Figure 6a shows the effect of changing the flow velocity at constant viscosity (μ = 2.5 mPa·s) and one cannot but notice the similar trend (but not magnitude) of the extensional efficiency, regardless of the flow velocity. The value of β dips just upstream of the first mixer before rapidly increasing to its maximum value just as the flow enters the mixer. This is mostly due to the fluid elements rotating slightly before being elongated as they have to pass through the volume between the crossbars of the mixer. The value of β then steadily decreases inside the mixer before the flow enters the 2nd mixer. In the second and subsequent mixer, the flow is characterized by an increase in β in approximately the first 1/3 of the volume, before its gradual decrease. The graph also shows that the value of β decreases as the flow exits the mixing section. However, the simulations showed that this decrease reaches a certain minimum before β increases steadily to 0.5 as the flow nears the exit of the pipe. This decrease is attributed to the propagation of the rotational flow downstream of the mixer. This effect will be further discussed in the section on helicity (Section 3.2.4).

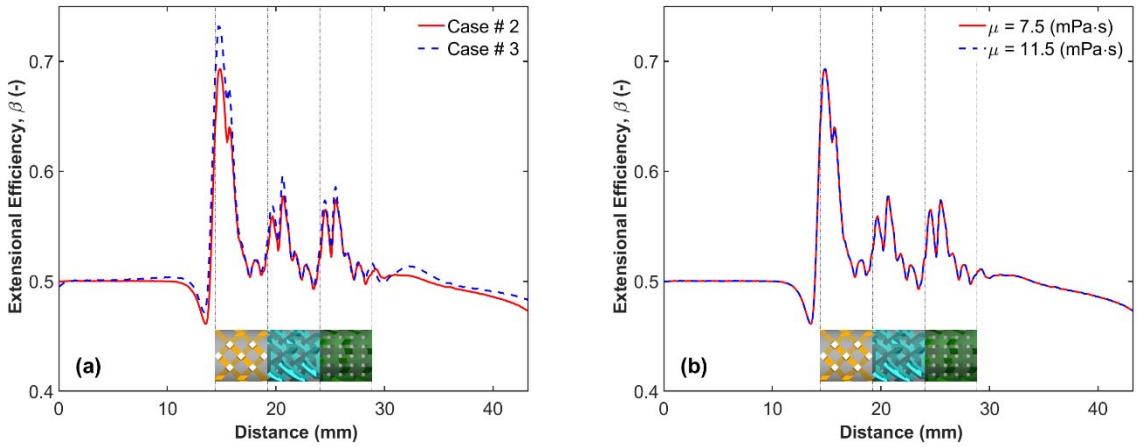


Figure 6: Extensional efficiency at different cross-section along the axial direction. (a) μ = 2.5 mPa·s, at Re$_h$ = 400 (Case #2) and Re$_h$ = 660 (Case #3); (b) Re$_h$ = 400, and μ = 7.5 (Case #4) and μ = 11.5 mPa·s (Case #5).

As mentioned earlier, a large value of β is required for the dispersion of fluid elements (Rauline et al., 1998), and the behavior observed in Figure 6 indicates that most of the breakage in multiphase flow systems would therefore be expected in the first part of the mixer.

Figure 6b shows the effect of changing the viscosity on the extensional efficiency at the same Re_h (= 400). As expected, viscosity had no effect on β as the trend is the same. It should be noted that, if plotted together, the trend of Case #2 (shown in Figure 6a) would also fall on top of those shown in Figure 6b.

3.2.3 Velocity profiles

The evolution of the velocity profiles along the axis of the flow are plotted in Figure 7 for cases #2 and 3. These profiles are plotted along the *x*-*z* plane at various distances downstream of the last mixer and were non-dimensionalized for both the velocity and radial location. The latter operation was performed by dividing the radial position by the pipe radius, whereby a value of 0 indicates the centerline of the pipe. The velocity magnitude was rendered dimensionless by dividing it by the centerline velocity at the inlet of the pipe according to Equation (12).

$$\langle U \rangle^* = \frac{\langle U_x \rangle}{\langle U_x \rangle|_{x=0,y=0,z=0}} \tag{12}$$

As previously mentioned, a fully developed velocity profile was imposed at the inlet of the pipe, as such, the velocity was divided by the maximum centerline velocity.

The dimensionless velocity profiles are plotted at 0.5*D*, 1*D*, 2*D* and 6*D* downstream of the last mixer element, respectively. In addition, the fully developed laminar flow velocity profile is overlaid on these graphs for ease of comparison.

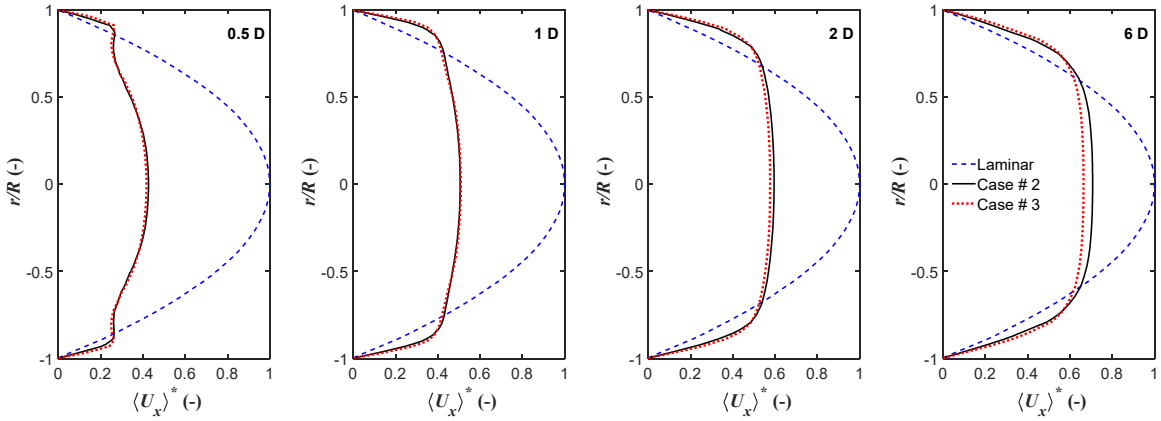


Figure 7: Normalized velocity profiles at different locations downstream of the third mixer element for cases # 2 and 3.

The effect of having the mixers can be clearly observed whereby the velocity profile remains much flatter than the fully developed laminar profile even at 6*D* downstream of the mixer. The flow exits the last mixer in the series with a very flat profile that is bulging near the wall and

around the centerline. Although it can be clearly observed from this series of profiles that the velocity profile attempts a slow return to its original form, the recovery is much slower at higher velocities. This can be clearly observed at the 6*D* distance from the last mixer where the profile at a higher velocity (Case # 3) is flatter than that at the lower velocity (Case # 2).

3.2.4 Helicity

The helicity is defined as the dot product of the vorticity and velocity vector. It is considered as a key parameter to quantify how the vorticity vector is transported by the velocity field thereby presenting the magnitude and direction of the helical flow (Regner et al., 2006).

$$H = \frac{\langle U_i \rangle \cdot \langle \omega_i \rangle}{|\langle U_i \rangle||\langle \omega_i \rangle|} \tag{13}$$

Habchi et al. (Habchi et al., 2013) normalized the helicity with respect to the product of the vorticity and velocity magnitudes as shown by Equation (13). This normalization makes it possible to compare helicities at different operating conditions.

Figure 8 shows the dimensionless helicity, H, on cross-sections at various distances downstream of the last mixer for cases #1, 2, and 3. The downstream locations correspond to the same conditions plotted earlier for the velocity profiles. It is very clear that the flow exits the mixing region with both clockwise and counter-clockwise swirls. The former quickly subside leaving only a counter-clockwise rotation being carried away further downstream of the mixer and is concentrated at the core of the flow. This explains the observed decrease in the value of the extensional efficiency, β, downstream of the last mixer. In other words, the core of the flow continues to be rotational which also provides an explanation for the observed flat velocity profiles in these regions. Figure 8 also presents the effect of changing the flow velocity on the magnitude of the helicity. As can be seen, the magnitude of the helicity is larger at larger flow velocities, which also explains the flatter velocity profile under those conditions farther downstream of the mixer (cf. Figure 7 at 6*D*).

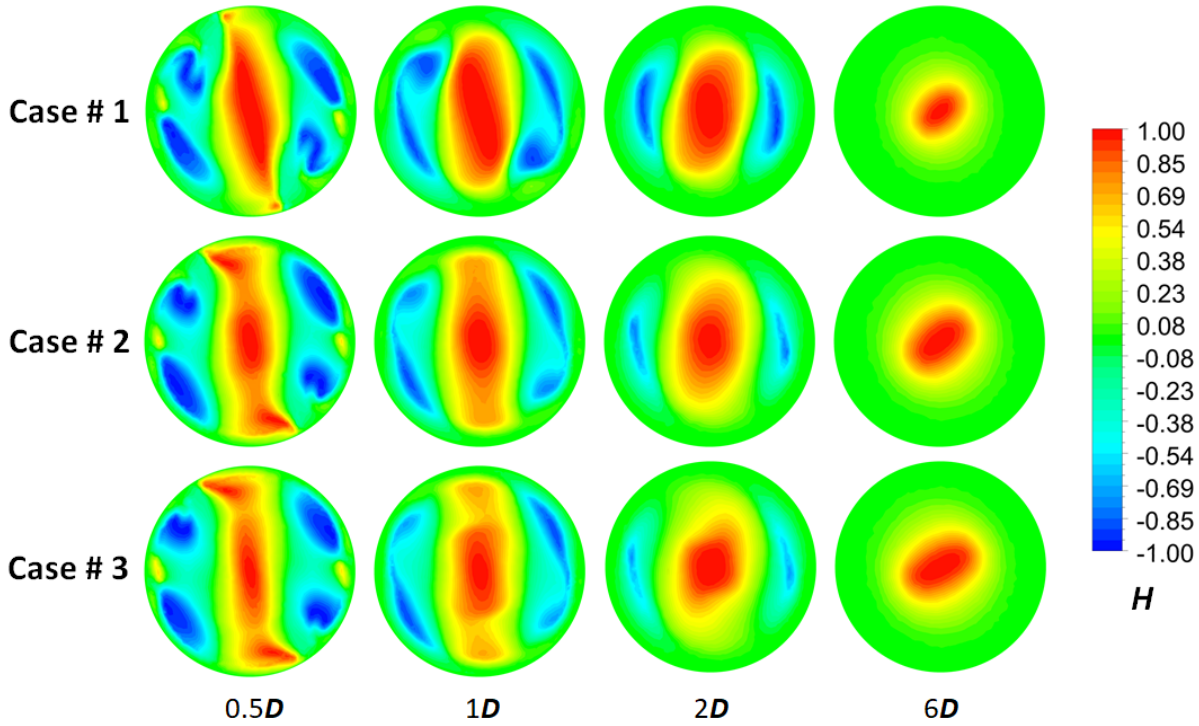


Figure 8: Contour plots of the normalized helicity, H, at various locations downstream from the last mixer for cases 1, 2, and 3.

3.2.5 Turbulence

The turbulence field was also studied in these mixers. This was accomplished by following the variation of the total dissipation rate of the flow. This total dissipation rate, $\varepsilon_{\mathrm{tot}}$, is the sum of the dissipation rate by the mean flow, ε_{m}, and the turbulent dissipation rate, ε_{t} (Forde, 2012; Lane, 2015). The definition of these various terms is shown below in equations (14) to (17).

$$\varepsilon_{\mathrm{tot}} = \varepsilon_{\mathrm{m}} + \varepsilon_{\mathrm{t}} \tag{14}$$

$$\varepsilon_{\mathrm{m}} = 2\nu \bar{S}_{ij} \bar{S}_{ij} \tag{15}$$

$$\varepsilon_{\mathrm{t}} = 2\nu \langle s'_{ij} s'_{ij} \rangle \tag{16}$$

$$s'_{ij} = \frac{1}{2}\left(\frac{\partial u'_i}{\partial x_j} + \frac{\partial u'_j}{\partial x_i}\right) \tag{17}$$

where $\bar{S}_{ij}$ and s'_{ij} are the mean and fluctuating rates of strain.

The rate of change of the average values of the three different energy dissipation rates are shown independently in Figure 9. In this figure, the mixing elements are overlaid on the charts to show the physical location of the mixers with respect to the data. Although the trends in all three subplots appear to be the same, the magnitude of each component is different. In general, the

energy dissipation rate increases exponentially as the flow enters the first mixing element where it fluctuates around a certain mean value. This fluctuation is due to the flow going through the changing cross-sections along the length of the mixer. Towards the exit of the mixing element, the value of the energy dissipation rate decreases sharply but goes through a second increase when the flow hits the following mixer. At the end of the mixing section, the value of the energy dissipation rate undergoes a sharp decrease followed by a gradual return to its value in an empty pipe. It can be easily discerned from Figure 9 that under the investigated flow conditions, the mean flow dissipation rate constitutes a major part of the total dissipation rate and hence omitting the contribution of the mean flow dissipation would seriously underestimate the total dissipation rate under similar conditions. This is best illustrated by comparing the total energy dissipation rate predicted by CFD simulations, $\varepsilon_{\mathrm{tot}}$, and the experimentally determined volume average values, $\varepsilon_{\mathrm{exp}}$, across one mixer element. This comparison is presented in Figure 10 in the form of a parity plot for the same conditions presented earlier in the pressure drop validation section. The experimental values were computed as volume average energy dissipation rates across one mixer using Equation (18), while the CFD values were extracted directly from Fluent®.

$$\varepsilon_{\mathrm{exp}} = \frac{\Delta p_{\mathrm{e}} \cdot U_{\mathrm{avg}}}{\rho \cdot L_{\mathrm{m}} \cdot \varphi} \tag{18}$$

As can be seen from Figure 10, a good match between these two values is obtained with the mean relative error being equal to ± 15.1%.

It should be noted that the highest pipe Re value investigated here is $\mathrm{Re}_{pipe} \approx 1{,}200$ which corresponds to a laminar flow in the empty pipe. The ratio of turbulent dissipation rate to mean flow dissipation rate is however expected to increase with an increase in the pipe Reynolds number with the contribution of the mean flow becoming less important towards highly turbulent conditions. It is worth adding that from these results and others conducted using 5 and more mixers in a series, it was clear that the average total energy dissipation rate per mixer becomes constant from the second mixer onwards with only the first mixer in the series showing a lower value of $\varepsilon_{\mathrm{tot}}$.

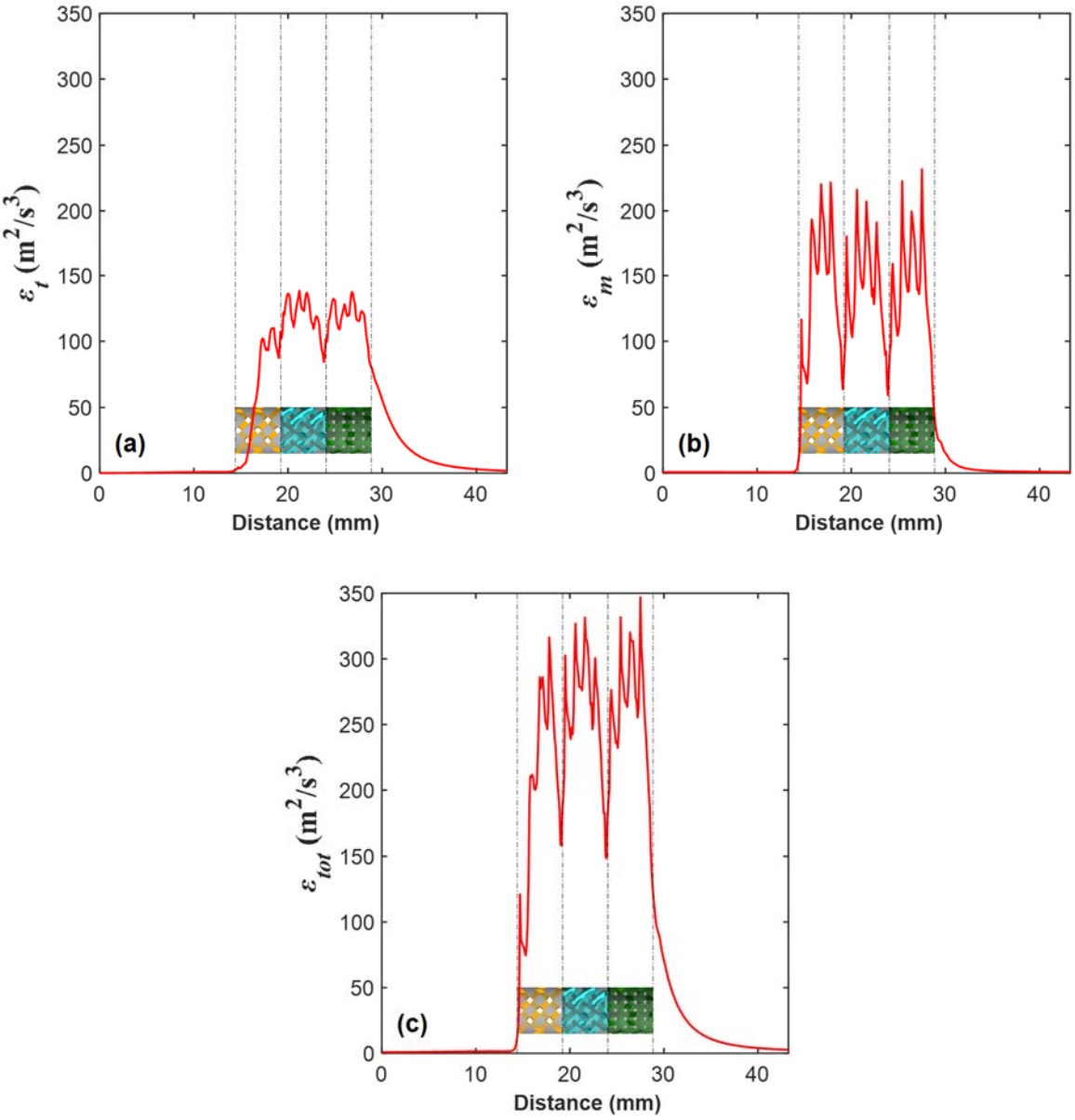


Figure 9: Variation of the energy dissipation rate along the length of the mixer for Case # 3. (a) turbulent energy dissipation rate; (b) mean flow dissipation rate; (c) total dissipation rate.

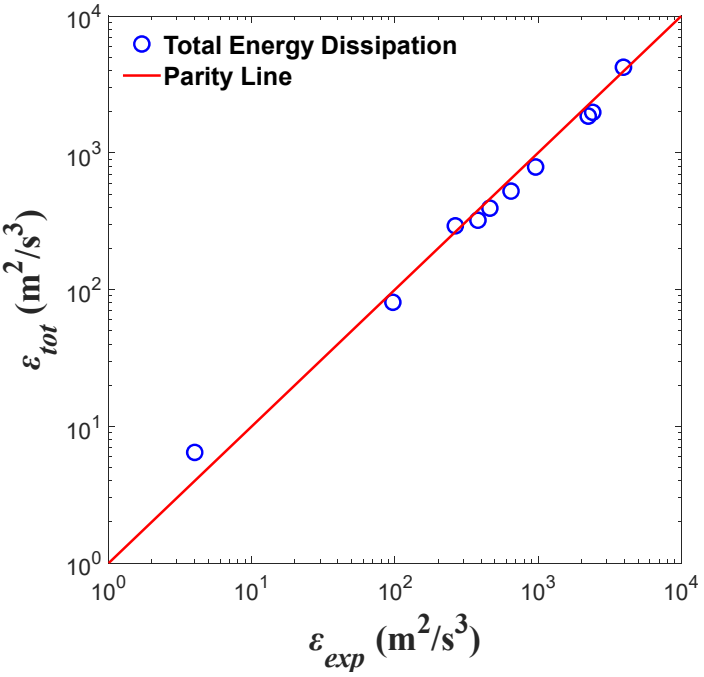


Figure 10: Parity plot between CFD predictions and experimentally determined average energy dissipation rates in the second mixing element.

Similarly to the energy dissipation rate, the kinetic energy of the flow can also be divided into contributions from turbulence and another from the mean flow. Accordingly, the total kinetic energy of the flow, k_{tot}, is the summation of the turbulent kinetic energy, k_t, and the mean flow kinetic energy, k_m. The variation of these three parameters is shown in Figure 11 where it is also clear that the contribution of the turbulent component is small compared to the mean flow component. The trends of the kinetic energy also show an exponential increase in its mean value when the flow passes through the first mixer and decreases as it nears its exit, however its value increases again as the flow enters the second mixer. The repetitive nature of the flow as it passes in the second and subsequent mixers is also clearly discerned in Figure 11 where the average value of the kinetic energy (due to the mean flow or the turbulent field) becomes almost repetitive after the second mixer.

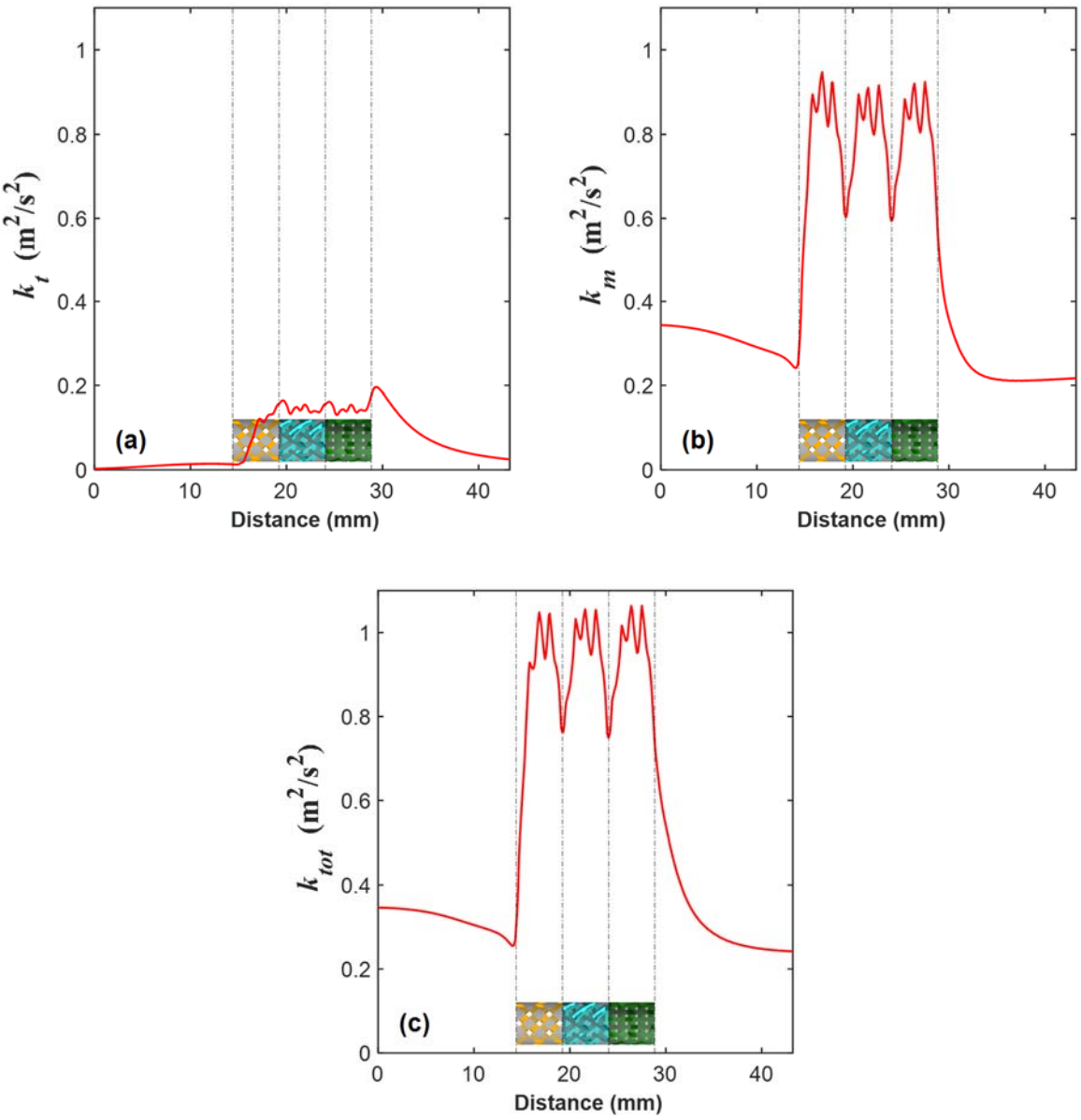


Figure 11: Variation of the mass-weighted average kinetic energy along the length of the mixer for Case # 3. (a) turbulent kinetic energy; (b) mean flow kinetic energy; (c) total kinetic energy.

4 Conclusions

A numerical investigation of single-phase flow through SMX+ mixers was presented here. The aim of this work was to shed light on the changes in the hydrodynamics of the flow as it passes through these mixers as no previous studies exist. Three mixer elements were employed in series with every mixer being rotated 45° to the previous one. The velocity field, extensional efficiency, helicity, and turbulence were carefully investigated under various flow velocities and viscosities. The numerical results were subjected to a grid independence study and validated

against experimentally measured pressure drop data. This data set spanned a wide spectrum of flow velocities and viscosities. The pressure drop predictions were found to fall on average within ± 13.8% of the experimental values.

Changing the flow viscosity showed no impact on the various parameters at the same value of Reynolds number. However, changing the flow velocity (for the same viscosity) had a much more pronounced effect.

The velocity field showed that the radial and tangential components of the velocity vector are of substantial magnitude inside the mixer where the flow cannot be considered as one-dimensional. This gives rise to regions with clockwise and/or counter-clockwise swirl rotation within the mixer which is an indication of good radial mixing of the fluid elements within the mixer. However, the strain rate distribution was found to be non-uniform within the mixer volume, with its highest values being on the solid walls of either the pipe or the mixer crossbars. Regions of low strain rates dominated the interior of the mixer and this was found in line with the findings of Liu et al. (Liu et al., 2006) who reported a similar behavior for the SMX mixers.

CFD simulations also showed that most stretching and elongation of fluid elements take place in the first part of the mixing element where the extensional efficiency quickly increases to its highest value before it quickly decreases as the flow passes through the mixer.

It was interesting to note that the value of the extensional efficiency continues to steadily decrease to values below 0.5 after the flow exits the last mixer element before it increases again further downstream. This was attributed to the propagation of the rotational flow downstream of the mixer which was best observed by means of the helicity. This latter parameter showed that the rotational nature of the flow was maintained to a considerable region downstream of the last mixer with the magnitude of the helicity being directly proportional to the flow velocity. The presence of this rotational core also explained the flatter velocity profiles at high flow velocities further downstream of the last mixer.

The turbulence field was also investigated by means of the mean values of the energy dissipation and kinetic energies. These results showed that the mean flow energy should not be disregarded at the conditions investigated in this work as they constitute the major part of the total energy dissipation rate or total kinetic energy.

Finally, it was found that various parameters and average values become almost constant from the second mixer onwards. This conclusion was reached from the current study and other simulations conducted with five (or more) mixers in series.

Acknowledgment

The authors would like to acknowledge the support of the University Research Board (URB) and the High-Performance Computing Unit at the American University of Beirut.

Nomenclature

D	Pipe diameter	mm
D_{h}	Hydraulic diameter	mm
H	Helicity	m/s^2
k_{m}	Mean kinetic energy	m^2/s^2
k_{t}	Turbulent kinetic Energy	m^2/s^2
k_{tot}	Total kinetic energy	m^2/s^2
L_{p}	Total Pipe length	mm
L_{m}	Mixer length	mm
L^*	Non-dimensional mixer length	–
N_{e}	Number of grid cells	–
p	Static pressure	Pa
$\bar{S}_{ij}$	Mean rate of strain tensor	(1/s)
s'_{ij}	Fluctuating rate of strain tensor	(1/s)
$\lvert\bar{S}_{ij}\rvert$	Magnitude of mean strain rate tensor	(1/s)
U_{avg}	Average velocity	m/s
U_i	Instantaneous velocity vector	m/s
$\langle U_i \rangle$	Mean velocity vector	m/s
$\langle U_i \rangle^*$	Normalized mean velocity vector	–
u'_i	Fluctuating velocity vector	m/s
R	Pipe radius	mm
r	Radial distance measured from the pipe center	mm
ΔP_{e}	Static pressure drop across a one mixer element	Pa
Greek symbols		
β	Extensional efficiency	–
ε_{m}	Dissipation rate of mean flow	m^2/s^3
ε_{t}	Dissipation rate of turbulent kinetic energy	m^2/s^3

$\varepsilon_{\mathrm{tot}}$	Total dissipation rate	m^2/s^3
ρ	Density	kg/m^3
$\overline{\Omega}_{ij}$	Mean vorticity tensor	(1/s)
$\left\|\overline{\Omega}_{ij}\right\|$	Magnitude of mean vorticity tensor	(1/s)
μ	Dynamic viscosity	Pa.s
μ_{t}	Turbulent viscosity	Pa.s
ν	Kinematic viscosity	m^2/s^2
ν_{t}	Turbulent Kinematic viscosity	m^2/s^2
φ	Porosity of the mixer	–
$\langle\omega_i\rangle$	Vorticity vector	(1/s)
Dimensionless Group		
Re_h	Hydraulic Reynolds number, $(\rho U D_{\mathrm{h}}/\mu\varphi)$	–
Re_{pipe}	Pipe Reynolds number, $(\rho U D/\mu)$	–
Abbreviations		
CFD	Computational Fluid Dynamics	
FVM	Finite volume method	
GCI	Grid Convergence Index	

References

Celik, I.B., Ghia, U., Roache, P.J., Freitas, C.J., Coleman, H., Raad, P.E., 2008. Procedure for estimation and reporting of uncertainty due to discretization in CFD applications. J. Fluids Eng. Trans. ASME 130, 0780011–0780014. https://doi.org/10.1115/1.2960953

Chabanon, E., Sheibat-Othman, N., Mdere, O., Valour, J.P., Urbaniak, S., Puel, F., 2017. Drop size distribution monitoring of oil-in-water emulsions in SMX+ static mixers: Effect of operating and geometrical conditions. Int. J. Multiph. Flow 92, 61–69. https://doi.org/10.1016/j.ijmultiphaseflow.2017.03.001

Coroneo, M., Montante, G., Paglianti, A., 2012. Computational fluid dynamics modeling of corrugated static mixers for turbulent applications. Ind. Eng. Chem. Res. 51, 15986–15996. https://doi.org/10.1021/ie300398z

de la Villéon, J., Bertrand, F., Tanguy, P.A., Labrie, R., Bousquet, J., Lebouvier, D., 1998. Numerical Investigation of Mixing Efficiency of Helical Ribbons. AIChE J. 44, 972–977. https://doi.org/10.1002/aic.690440423

Forde, O.O., 2012. Analysis of the Turbulent Energy Dissipation 56.

Ghanem, A., Lemenand, T., Della, D., Peerhossaini, H., Della Valle, D., Peerhossaini, H., Della, D., Peerhossaini, H., 2014. Static mixers : Mechanisms , applications , and characterization methods – A review. Chem. Eng. Res. Des. 92, 205–228. https://doi.org/10.1016/j.cherd.2013.07.013

Habchi, C., Harion, J., Russeil, S., Bougeard, D., Hachem, F., Elmarakbi, A., 2013. Chaotic mixing by longitudinal vorticity. Chem. Eng. Sci. 104, 439–450. https://doi.org/10.1016/j.ces.2013.09.032

Haddadi, M.M., Hosseini, S.H., Rashtchian, D., Olazar, M., 2020. Comparative analysis of different static mixers performance by CFD technique : An innovative mixer. Chinese J. Chem. Eng. 28, 672–684. https://doi.org/10.1016/j.cjche.2019.09.004

Hinze, J.O., 1959. Turbulence: an introduction to its mechanism and theory. McGraw-Hill, New York.

Hirschberg, S., Koubek, R., F.Moser, Schöck, J., 2009. An improvement of the Sulzer SMX TM static mixer significantly reducing the pressure drop. Chem. Eng. Res. Des. 87, 524–532. https://doi.org/10.1016/j.cherd.2008.12.021

Jegatheeswaran, S., Ein-Mozaffari, F., Wu, J., 2018. Process intensification in a chaotic SMX static mixer to achieve an energy-efficient mixing operation of non-newtonian fluids. Chem. Eng. Process. Process Intensif. 124, 1–10. https://doi.org/10.1016/j.cep.2017.11.018

Jeong, J., Hussain, F., 1995. On the identification of a vortex. J. Fluid Mech. 285, 69–94.

Kresta, S.M., Etchells, A.W., Dickey, D.S., Atiemo-Obeng, V.A. (Eds.), 2016. Advances in Industrial Mixing - A companion to the Handbook of Industrial Mixing, 1st ed. John Wiley & Sons.

Lane, G., 2015. Prediction the energy dissipation rate in a mechanically stirred tank. Elev. Int. Conf. CFD Miner. Process Ind. 7.

Lebaz, N., Sheibat-Othman, N., 2019a. Modeling Emulsification in Static Mixers: Equilibrium Correlations versus Population Balance Equations. Chem. Eng. Technol. 42, 1691–1701. https://doi.org/10.1002/ceat.201900109

Lebaz, N., Sheibat-Othman, N., 2019b. A population balance model for the prediction of

breakage of emulsion droplets in SMX+ static mixers. Chem. Eng. J. 361, 625–634. https://doi.org/10.1016/j.cej.2018.12.090

Leclaire, S., Vidal, D., Fradette, L., Bertrand, F., 2020. Validation of the pressure drop – flow rate relationship predicted by lattice Boltzmann simulations for immiscible liquid – liquid flows through SMX static mixers. Chem. Eng. Res. Des. 3, 350–368. https://doi.org/10.1016/j.cherd.2019.10.035

Liu, S., Hrymak, A.N., Wood, P.E., 2006. Design modifications to SMX static mixer for improving mixing. AIChE J. 52, 150–157. https://doi.org/10.1002/aic.10608

Manas-Zloczower, I., 1994. Studies of Mixing Efficiency in Batch and Continuous Mixers. Rubber Chem. Technol. 67, 504–528.

Meijer, H.E.H., Singh, M.K., Anderson, P.D., 2012. On the performance of static mixers: A quantitative comparison. Prog. Polym. Sci. 37, 1333–1349. https://doi.org/10.1016/j.progpolymsci.2011.12.004

Pianko-Oprych, P., Jaworski, Z., 2010. Prediction of liquid – liquid flow in an SMX static mixer using large eddy simulations. Chem. Pap. 64, 203–212. https://doi.org/10.2478/s11696-009-0112-9

Rauline, D., Le Blévec, J.M., Bousquet, J., Tanguy, P.A., 2000. A comparative assessment of the performance of the Kenics and SMX static mixers. Chem. Eng. Res. Des. 78, 389–396. https://doi.org/10.1205/026387600527284

Rauline, D., Tanguy, P.A., Le Blévec, J.M., Bousquet, J., 1998. Numerical investigation of the performance of several static mixers. Can. J. Chem. Eng. https://doi.org/10.1002/cjce.5450760325

Regner, M., Östergren, K., Trägårdh, C., 2006. Effects of geometry and flow rate on secondary flow and the mixing process in static mixers-a numerical study. Chem. Eng. Sci. 61, 6133–6141. https://doi.org/10.1016/j.ces.2006.05.044

Thakur, R.K., Vial, C., Nigam, K.D.P., Nauman, E.B., Djelveh, G., 2003. Static mixers in the process industries - a review. Chem. Eng. Res. Des. 81, 787–826. https://doi.org/10.1205/026387603322302968

Theron, F., Le Sauze, N., Ricard, A., 2010. Turbulent liquid-liquid dispersion in sulzer SMX mixer. Ind. Eng. Chem. Res. 49, 623–632. https://doi.org/10.1021/ie900090d

Theron, F., Sauze, N. Le, 2011. Comparison between three static mixers for emulsification in turbulent flow. Int. J. Multiph. Flow 37, 488–500. https://doi.org/10.1016/j.ijmultiphaseflow.2011.01.004

Vikhansky, A., 2020. CFD modelling of turbulent liquid–liquid dispersion in a static mixer. Chem. Eng. Process. Process Intensif. 149, 107840. https://doi.org/10.1016/j.cep.2020.107840